



A near-wake survey of an Ahmed body comparing low- & high-fidelity numerical models with experiments

Wassim Zeidan, Nicolas Mazellier, Emmanuel Guilmineau, Pierre-Yves Passaggia, Azeddine Kourta

► To cite this version:

Wassim Zeidan, Nicolas Mazellier, Emmanuel Guilmineau, Pierre-Yves Passaggia, Azeddine Kourta. A near-wake survey of an Ahmed body comparing low- & high-fidelity numerical models with experiments. European Journal of Mechanics - B/Fluids, 2023, 101, pp.195-208. 10.1016/j.euromechflu.2023.05.002 . hal-04281918

HAL Id: hal-04281918

<https://hal.science/hal-04281918>

Submitted on 15 Nov 2023

HAL is a multi-disciplinary open access archive for the deposit and dissemination of scientific research documents, whether they are published or not. The documents may come from teaching and research institutions in France or abroad, or from public or private research centers.

L'archive ouverte pluridisciplinaire **HAL**, est destinée au dépôt et à la diffusion de documents scientifiques de niveau recherche, publiés ou non, émanant des établissements d'enseignement et de recherche français ou étrangers, des laboratoires publics ou privés.

A near-wake survey of an Ahmed body comparing low- & high-fidelity numerical models with experiments

Wassim Zeidan^a, Nicolas Mazellier^a, Emmanuel Guilmineau^b, Pierre-Yves Passaggia^a and Azeddine Kourta^a

^aUniv. Orléans, INSA CVL, PRISME, EA 4229, 8 Rue Léonard de Vinci, Orléans,, F45072, France

^bLHEEA, CNRS 6598, Ecole Centrale de Nantes (ECN - CNRS) CNRS, 1 rue de la Noë, Nantes, F44321, France

ARTICLE INFO

Keywords:

Bluff-body flows
turbulence modelling
Aerodynamic drag
computational fluid dynamics
wind-tunnel experiments


ABSTRACT

A full-scale square-back Ahmed body is analysed experimentally and numerically for a free-stream flow velocity of 45m/s corresponding to a Reynolds number $Re_H = 7.7 \times 10^5$. Numerical simulations are performed for matching inflow conditions and different turbulence models. The main goal of this study is to examine the effectiveness of the Delayed Detached Eddy Simulations and the Reynolds Averaged Navier Stokes $k - \omega$ SST turbulence model to capture the mean flow physics. Local and global aerodynamic parameters are compared with experimental results, including boundary-layer parameters evolving over the roof, the wake characteristics, the shear layer, and the mass entrained into the wake. A particularly good agreement is found between the experiment and the DDES. An in-depth analysis of the shear-layer growth, mass-entrainment and momentum budget analyses along the recirculation region interface, allow for identifying and quantifying the differences in predicting drag and the mechanisms at stake between the different approaches. The momentum budget, performed on the experimental data shows that pressure can be accurately obtained from experiments and closely follows that computed from high-fidelity numerical simulations. These results confirm the effectiveness of DDES in studying flows at high Reynolds numbers. The mass/momentum budget along the recirculation-region interface is also found as a possible mean to quantify road vehicle's aerodynamic performances, naturally extending to more complex geometries.

1. Introduction

The transportation industry, and in particular, road vehicles, remain one of the main contributors to global energy consumption and pollutant emissions. Car manufacturers must therefore comply with environmental regulations such as CO₂-emissions standards which are becoming increasingly strict. Reducing the aerodynamic drag through flow control strategies stands as an appealing solution to comply with these policies but performing statistically converged numerical simulations at such high Reynolds numbers remains a challenge. Ahmed, Ramm and Faltin (1984) introduced a simplified yet ubiquitous vehicle design, akin to a wide range of commercial road vehicles shapes. The objective of various experimental works including Spohn (2002); Beaudoin, Cadot, JI, Gosse, Paranthoen, Hamelin, Tissier, Allano, Mutabazi, Gonzales and Je (2004); Conan, Anthoine and Philippe (2011); Grandemange, Gohlke and Cadot (2013c); Volpe, Devinant and Kourta (2015), numerical studies such as Krajnović and Davidson (2005); Lucas, Cadot, Herbert, Parpais and Delery (2017); Hesse and Morgans (2021) regarding square-back Ahmed bodies, and Serre, Minguez, Pasquetti, Guilmineau, Deng, Kornhaas, Schäfer, Fröhlich, Hinterberger and Rodi (2013); Guilmineau, Deng, Quentey and Visonneau (2016) for slanted Ahmed body is the study of the near-wake flow at high Reynolds number. Nevertheless, reattachment happens relatively fast since the frontal body shape is designed to avoid a large separation (Ahmed et al., 1984). The afterbody separation generates a very large recirculation bubble downstream of the body, contributing to the dominant part of the drag, knowing that 50% to 70% of the total drag is produced by the rear part of the vehicle. From this issue, we focus our analysis on the near-wake region behind an Ahmed body. The aim is to provide a generic approach to diagnose drag and address momentum budgets in the case of three-dimensional bluff bodies.

The near wake is characterised by a recirculation region which can be delimited from the outer flow using two different flow characteristics; (i) the recirculating streamline closest to the outer flow, known as the Dividing Streamline

 nicolas.mazellier@univ-orleans.fr (N. Mazellier)

ORCID(s): 0000-0002-4344-9671 (N. Mazellier); 0000-0001-9070-093X (E. Guilmineau); 0000-0002-3607-7224 (P. Passaggia); 0000-0003-0799-9251 (A. Kourta)

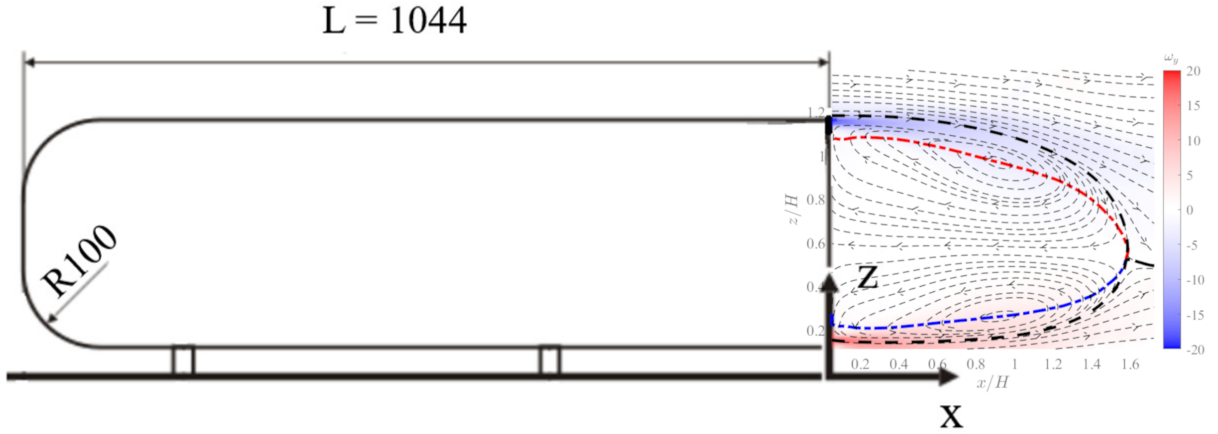


Figure 1: Sketch of the flow and wake geometry of an ahmed body showing the dividing streamline interface (DSI) in black with dashed lines and the recirculation region interface (RRI) with a (red-blue) dashed-dotted line. The colour background shows the vorticity non-dimensionalised with the free-stream velocity U_∞ and the height of the body H (adapted from Passaggia et al. (2021)).

Interface (DSI) (Passaggia et al., 2021) shown in black in figure 1 and (ii), the surfaces where the streamwise velocity is null (Stella, Mazellier and Kourta, 2017), known as the Recirculating-Region Interface (RRI) shown in red-blue in figure 1. Note that in the case of a wake, both the DSI and the RRI originate and terminate at the separation and the saddle point closing the recirculation bubble respectively. These generic interfaces can therefore be used to perform momentum budgets and link the topology of the near wake and the physical quantities of the flow to the forces acting upon the vehicle. Characterising drag can be therefore linked simultaneously to a geometric problem (i.e. the topology of the near wake) and a physical problem (i.e. estimating mechanical loads). The geometric problem aims at understanding the topological features of the wake. A particularly important quantity for a momentum budget analysis is the local slope of the interface which, in two dimensions, links the spatial derivatives and can be readily obtained from differential calculus as $dz = dz/dx|_{S_i} dx = \kappa dx$, where κ is the local interface's slope and S_i is the surface of the RRI or the DSI. The slope allows for linking physical quantities projected along the vertical direction with the horizontal contributions in the budget and reduces the momentum budget to a single equation linking the topology to the physical quantities. An interesting feature of both the RRI and the DSI is that the mean flow contributions naturally cancel when considering the budget for the drag force acting at the base of the vehicle. Whence, the budget along either the DSI and the RRI in the case of a 2D flow reduces to

$$F_{p,b} = \int_{S_i} P + \langle u'^2 \rangle dz + \int_{S_i} \langle u'w' \rangle dx = \int_{S_i} \kappa \left(P + \langle u'^2 \rangle \right) + \langle u'w' \rangle dx,$$

where $F_{p,b}$ is the pressure contribution to the drag force at the base of the vehicle per spanwise unit length, P is the mean pressure, while primed quantities denote turbulent quantities. Note that the RRI allows for computing the mass entrained across the recirculation region while this quantity naturally cancels when considering the DSI. In addition, the RRI is well defined for three-dimensional flows, contrary to the DSI. In this paper, we therefore use the RRI in order to analyse the flow in the near wake of an Ahmed body at a high Reynolds number for both numerical simulations and laboratory experiments for a quantitative comparison.

A remarkable body of work regarding high-fidelity simulations of the flow around squared-backed Ahmed body at high Reynolds number has been reported by Lucas et al. (2017); Dalla Longa, Evstafyeva and Morgans (2019); Evstafyeva, Morgans and Dalla Longa (2017); Hesse and Morgans (2021), regarding large-eddy simulations and wall-modelled large-eddy simulations. In these studies, the authors analysed the role of the modelling strategy on the the dynamics. Nevertheless a thorough analysis comparing experiments and simulations of the same body is still lacking. In particular, systematic approaches including global budgets to analyse the near-wake features have yet to make consensus.

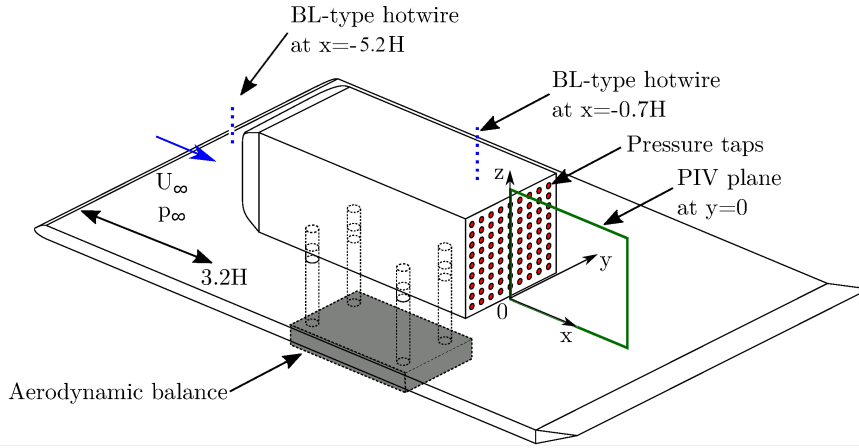


Figure 2: Sketch of the experimental setup.

Thus, the importance of the simulation presented in this article is the high Reynolds number, close to one million, which replicates a wind-tunnel experiment characteristics from the incoming boundary layer to the geometry of the near wake. At such high Reynolds numbers, well-resolved large-eddy simulations (Dalla Longa et al., 2019) are out of scope since the necessary simulation time to captures several wake reversals is too computationally intensive. Similar to Hesse and Morgans (2021), we use an intermediate approach such as delayed-detached-eddy simulations (Guilmineau et al., 2016; Guilmineau, B., Leroyer, Queutey, Visonneau and Wackers, 2018) over extensive simulation times to make sure that the temporal statistics of the mean flow are well converged. Besides, coupling between experimental and simulation analysis should allow for a more precise understanding of the flow physics. Thus, we report a complete analysis of the boundary layer developing over the roof, together with a mass and a momentum budget in the near wake in order to evaluate the quality of the mean field between experiments, high-fidelity numerical simulations and a standard Reynolds-averaged Navier-Stokes approach, using the RRI for the analysis.

The paper is organised as follows, §2 provides details about the experimental setup, §3 details the numerical strategy, and §4 provides a summary of the mathematical strategy to analyse the flow. Results are summarised and compared in §5 while conclusions are drawn in §6.

2. Experimental Setup

The experiment was performed at PRISME laboratory in Orleans University (France) in the wind tunnel of test section $2 \times 2 \text{ m}^2$ wide, and 5 m long. The model is a full-scale Ahmed body (Ahmed et al., 1984), with length $L = 1044 \text{ mm}$, width $W = 389 \text{ mm}$, height $H = 288 \text{ mm}$, ground clearance $h = 45 \text{ mm}$ (15% of the model height), within a blockage of 2.8%. The model was mounted via a plate located 0.47 m from the ground. The x-axis is aligned with the streamwise direction, the z-axis is vertical and positive upwards (as shown in figure 2). The origin is at the bottom of the base of the model at the mid wheelbase. An external strain gauge balance was used to measure the aerodynamic forces, located under the working section of the tunnel. The chosen sampling frequency is 1kHz but the dynamic response of the balance is 1Hz. The Ahmed body is linked to a six-components strain gauge balance through its feet, avoiding any contact with the ground. We focus here on the drag force D . The drag coefficient is measured with a 0.5% precision and is well within the range reported in the literature for a similar geometry and flow condition (Volpe et al., 2015; Lucas et al., 2017). Note that the same setup was studied in Passaggia et al. (2021) to analyse the effect of free-stream turbulence on the wake but for a slightly lower free-stream velocity and details about the experimental setup are shown in figure 1.

The pressure at the base was measured by covering the back-square face with a grid of 81 pressure taps connected through 600 mm long vinyl tubes, with an internal diameter $d = 1.56 \text{ mm}$, and with a manufacturer quoted accuracy of $\pm 6 \text{ Pa}$. Furthermore, pressure taps were located with a fine distribution close to the surface edges. In addition, two MicroDAQ pressure scanners were used with a sampling frequency of 50Hz. Note that the temperature in the test section was 38°C and that the kinematic viscosity of air was computed accordingly. In addition, two dimensional PIV

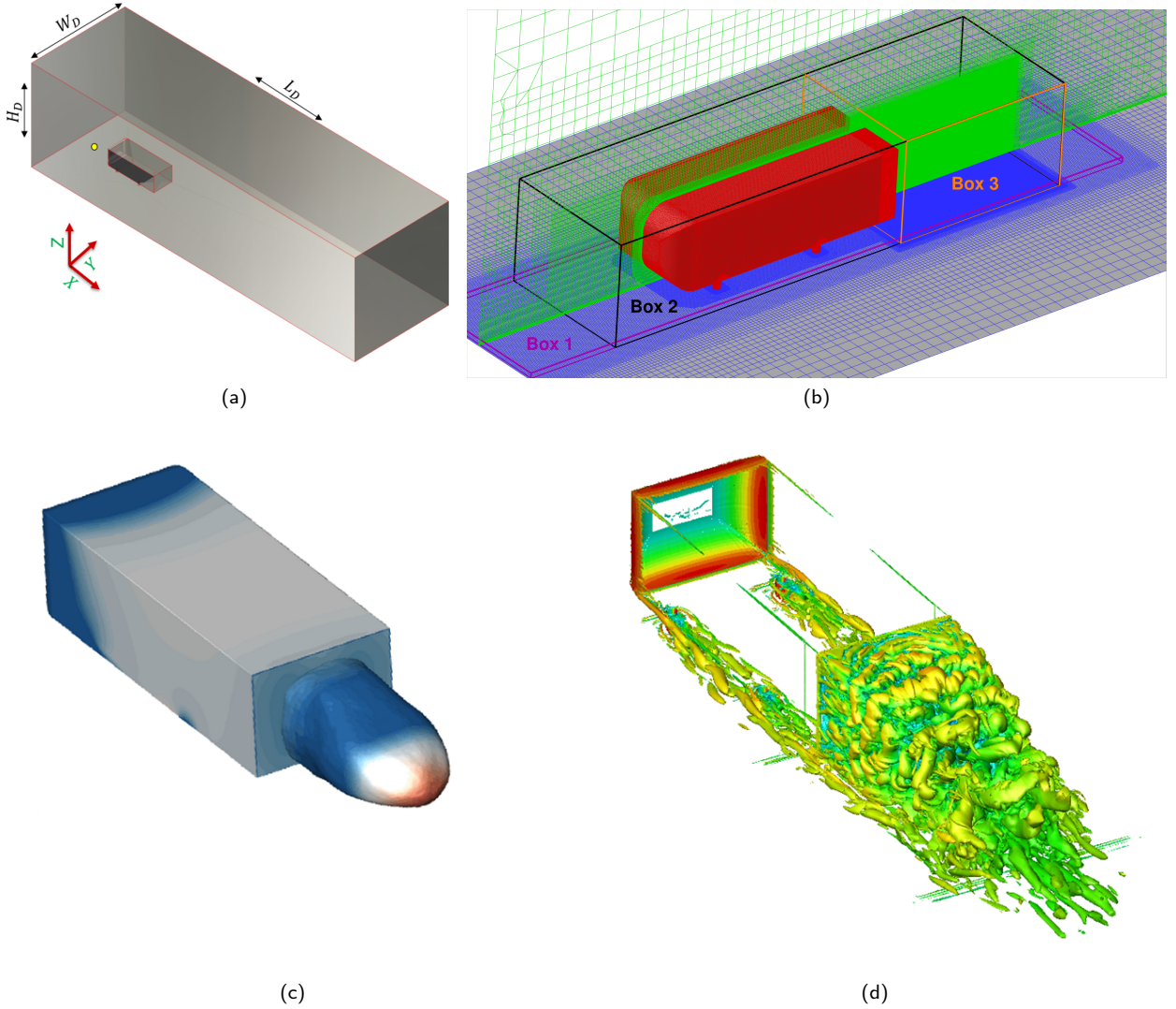


Figure 3: (a) Computational domain characterised by $L_D = 13.2L$, $W_D = 1.9L$ and $H_D = 1.7L$, the yellow dot shows the location where boundary-layer measurements were taken in the experiments. (b) The mesh specialized by three added boxes, box 1 covers the whole model while box 2 covers the under body area and box 3 is further refined in the near wake, downstream the body. (c) Mean recirculation region interface defined ($U(x_i) = 0$) coloured with the mean pressure computed from the DDES and (d) an instantaneous snapshot of the DDES coloured by means of the instantaneous horizontal velocity.

was performed using a LaVision system to analyse the topology of the near wake in the $X - Z$ mid plane, at $Y=0$, the image size is $392 \times 603 \text{ mm}^2$ with a spatial resolution of 2 mm for each vector. Measurements were acquired at a frequency of 2.49 Hz. The data were processed using the DPIVSoft toolbox (see (Passaggia, Chalamalla, Hurley, Scotti and Santilli, 2020) and Meunier and Leweke (2003)). Further details regarding PIV can be found in Passaggia et al. (2021).

3. Numerical simulations

3.1. Flow solver

The ISIS-CFD flow solver, uses an incompressible unsteady Reynolds-averaged Navier-Stokes (URANS) method. The solver is based on a finite-volume method to build the spatial discretization. The unstructured discretization is face

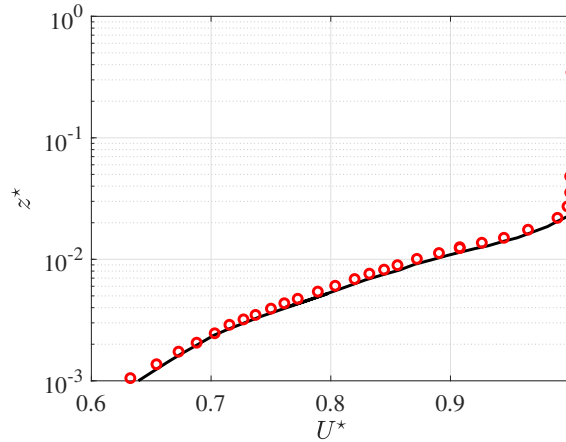


Figure 4: Comparison of the time-averaged boundary-layer profile measured at $x = -1.5H$ from the front part of the body for the simulations (continuous line) and experiment (symbols).

based with adaptive mesh refinement strategies. A second-order backward difference scheme is used for the temporal discretisation. A centred scheme is used for the diffusion terms whereas the convective fluxes use a blended scheme (i.e. 95% central differences and 5% upwind differences for the hybrid RANS-LES model, or 80% central and 20% upwind for the RANS model (Krajnović and Sarmast, 2010)). Two fully unstructured hexahedral meshes were constructed using HEXPRESS, the first with 32 million cells and the second with 56 million cells. The convergence was chosen referring to physical parameters such as the drag coefficient, the recirculating region length alongside the experiment. To compromise between the computational costs and accuracy, a mesh study was conducted and the first mesh was considered. Snapshots are shown in figure 3b for illustration.

In this paper, two turbulence models are used: the RANS $k-\omega$ SST Menter (1994) and the Delayed Detached Eddy Simulation (DDES). The DDES model is a SST-based DDES proposed by Gritskevich, Garbaruk, Schütze and Menter (2012). The benefits of DDES is the ability to split the computational domain into two zones; Near-wall regions are covered by the first zone where the standard RANS equations are resolved while a LES approach is used in the second zone. The velocity field is obtained from the momentum conservation equations and the pressure field is extracted from the mass conservation constraint or continuity equation, transformed into a pressure-equation. The pressure equation is obtained by the Rhie and Chow (1983) interpolation. The momentum and pressure equations are solved in a segregated manner as in the simple coupling procedure (Issa, 1986).

The same simplified vehicle model (same as used in the experiments) is discretised on a computational domain with dimensions $13.2L \times 1.7L \times 1.9L$ (see figure 3a). The upstream distance between the inlet and the body were chosen, and at a position $1.5H$ upstream the front part of the body. A boundary layer measurements is taken and compared with experiment. Figure 4 shows the boundary-layer comparison between experiments and simulation at a distance $1.5H$ in front of the Ahmed body. The figure shows a comparable result between the simulation and experiment at velocity equal to 45 m/s, which validates the size of the computational domain.

Boundary conditions were chosen as follows, a 45 m/s inlet was imposed, a no-slip condition was considered for the body and the road to enable boundary-layer growth. In order to capture near-wall features, a refinement was performed defining three boxes covering the whole body and zooming on the rear part in which the cell length was 1.8mm. The coordinate axis system was defined similar to the experiment to facilitate the comparison (see figure 3a), with an origin at the mid-base bottom part of the body. The non-dimensional time step $\Delta t^* = 0.1$ captures the boundary layer correctly and is higher than the time step calculated by $\Delta t^* = \Delta t U_\infty / H$, with $\Delta t = \Delta x / U_n$, where U_n is the average velocity in the wake region. Note that 480 processors were used, with a computational time $t^* = 1250$, where $t^* = t U_\infty / H$, t is the physical time in seconds, U_∞ is the free-stream velocity and H is the height of the body. The resulting mean flow is shown in figure 3c while a snapshot of the turbulent flow is depicted in figure 3d by means of the Q -criterion coloured with the instantaneous horizontal velocity.

4. Mathematical tools

In what follows, the flow quantities are non-dimensionalized using the height of the body H and the free-stream velocity U_∞ such that

$$t^\star = tU_\infty/H, \quad x_i^\star = x_i/H, \quad u_i^\star = u_i/U_\infty, \quad \text{and} \quad p^\star = p/\rho U_\infty^2, \quad (1)$$

unless specified otherwise. Note that ρ is the density of the fluid. Further, the analysis follows a Reynolds-Averaged Navier-Stokes (RANS) decomposition for the analysis between a mean and a fluctuation such that

$$(u_i, p) = (U_i(x_i) + u'_i(x_i, t), P(x_i) + p'(x_i, t)). \quad (2)$$

The time-averaged Navier-Stokes that is used throughout this study writes in non-dimensional form

$$U_j^\star \frac{\partial U_i^\star}{\partial x_j^\star} = -\frac{\partial P^\star}{\partial x_i^\star} - \frac{\partial}{\partial x_j^\star} \left(\langle u'_i u'_j \rangle^\star - \frac{1}{Re_H} \left(\frac{\partial U_i^\star}{\partial x_j^\star} + \frac{\partial U_j^\star}{\partial x_i^\star} \right) \right), \quad (3)$$

where $Re_H = U_\infty H/\nu$ is the Reynolds number kept nearly constant at $Re_H \approx 7.7 \times 10^5 \pm 1\%$ throughout this study. Note that the viscous term on the right-hand side of equation (3) is negligible and we do not consider its contribution hereinafter.

Mean pressure reconstruction of $P(x_i, z)$ is performed in the experiment in order to quantify the role of the mean pressure and Reynolds stresses in a momentum budget. The procedure first solves (3), which is akin to solving the Poisson problem

$$\nabla^2 P^\star = -\frac{\partial}{\partial x_j^\star} \left(\frac{\partial}{\partial x_i^\star} (U_i^\star U_j^\star + \langle u'_i u'_j \rangle^\star) \right), \quad (4)$$

but in a least-square sense (Harker and O'Leary, 2008; Harker and O'Leary, 2013; Passaggia et al., 2020), to obtain a first guess of the static pressure P^0 and then uses the pressure taps at the base of the body (at $y = 0$) to compute the static pressure. The true pressure P^\star is recovered using the adjoint method derived in Shanmughan, Passaggia, Mazellier and Kourta (2020), and adapted from Passaggia et al. (2021) for the boundary conditions.

Note that in the case of a symmetrised flow with respect to $y = 0$, the missing out-of-plane components of the velocity for the PIV are not problematic since the mean transverse v' -component of the flow is null by construction in the $(x - z)$ plane for the symmetrised flow while the transverse Reynolds-stress tensor gradient (i.e. $\partial_y \langle u'v' \rangle^\star$) has a negligible contribution in the recirculation region as will be shown later. The pressure reconstruction therefore makes little assumptions and is essentially dependent on the quality of the measurements.

5. Results and comparisons

5.1. Boundary-layer analysis

The boundary layer thickness, δ can be defined as the distance from the wall to the point where the mean streamwise velocity approaches 99% of the local free-stream velocity U_∞ . More interesting for this comparison is the displacement and the momentum thicknesses defined as

$$\delta^\star = \int_0^\infty \left(1 - \frac{U}{U_\infty} \right) dz \quad \text{and} \quad \theta = \int_0^\infty \frac{U}{U_\infty} \left(1 - \frac{U}{U_\infty} \right) dz, \quad (5)$$

where δ^\star is linked to the flow-rate deficit inside the boundary layer while θ is directly related to the skin-friction coefficient $C_f = 2\tau_w/\rho U_\infty^2$. The shape factor is given by $H_{sf} = \delta^\star/\theta$ and allows for a first assessment of the state of the boundary layer. The Reynolds number based on the momentum thickness $Re_\theta = U_\infty \theta/\nu$ while the non-dimensional parameter for the pressure gradient writes $\beta = (\delta^\star/\rho u_\tau) \partial P^\star / \partial x^\star$. The displacement and momentum thickness were evaluated using a trapezoidal rule. The boundary layer measurements were specified 12 cm (i.e. $x^\star = -0.7$) upstream the top trailing edge of the body, over the roof. The origin is set at the mid-bottom of the body base, shown in figure 1. Hence, several points were acquired to measure the boundary-layer properties using a single-component hot wire with a sampling frequency of 60 kHz. However, due to the limitation in the experimental setup, a minimum distance

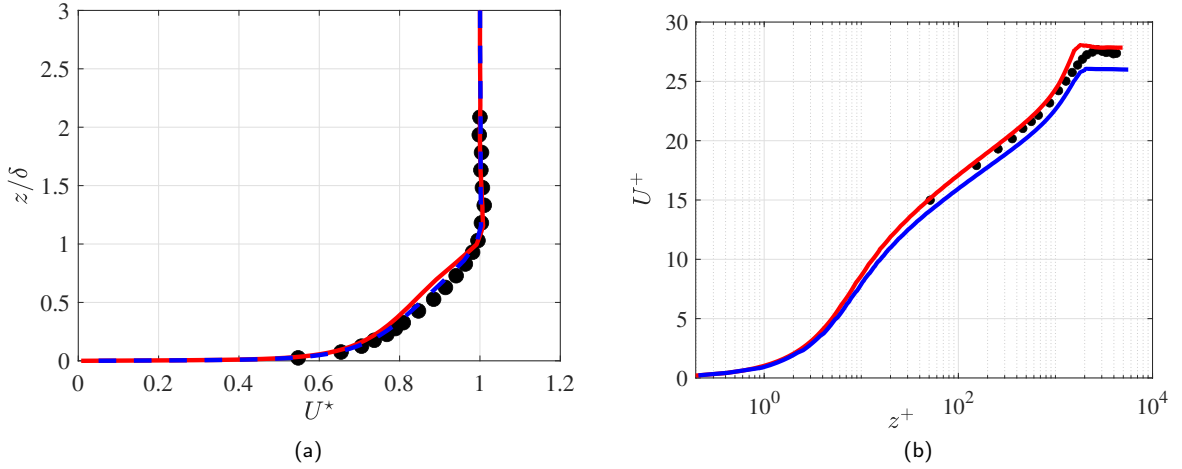


Figure 5: Mean velocity profile along the z -axis normalised in (a) by the free stream velocity and the boundary-layer thickness δ . (b) Same profile normalised using the friction velocity u_τ and the friction height $z_f = \nu/u_\tau$. The DDES is shown in red, the RANS in blue, and the experiment by means of symbols.

	$U_\infty (m/s)$	δ/H	δ^*/H	θ/H	H_{sf}	Re_θ	β
Experiment	45	0.069	0.0097	0.0076	1.29	5420	-0.26
DDES	44.4	0.055	0.01	0.0072	1.37	5307	-0.22
$k - \omega$ SST	43.9	0.059	0.01	0.0072	1.36	5256	-0.1

Table 1

Boundary-layer characteristics from experimental and simulation data.

of 0.5 mm from the wall remained insufficient to enter the viscous sub-layer. Experimental and simulation results are reported in table 1. The boundary layer can be considered as fully turbulent, since both conditions $Re_\theta > 3000$ and $H_{sf} > 1.2$ are met but it should be noted that the boundary layer may have not reached equilibrium since $H_{sf} \approx 1.3$.

Figure 5a shows the mean streamwise velocity as a function of the wall-normal distance z from the roof of the body normalized with the free-stream velocity and the boundary layer thickness respectively. A good match between experiments and the simulations (for both turbulence models) is observed. A slight difference is noticed along the evolution of the streamwise velocity profile between the experiment and simulations (see figure 5a). In a similar study, Trip and Fransson (2017) report velocity profiles distinctions because of the state of the turbulent boundary layer which is expected since $H_{sf} \approx 1.3$. As a result, both cases (experiments and simulation) demonstrate a turbulent boundary layer.

The inner region of the boundary layer is defined from $z = 0$ up to $z = 0.1\delta$ (Pope, 2001). In this region, the wall-shear stress influences the flow. In the case of a zero-pressure gradient boundary layer over a flat plate, the advection terms are negligibly and a balance can be observed between the viscous and the turbulent shear stress. The flow inside the turbulent boundary layer can be rescaled based on the friction velocity u_τ but measuring directly the friction velocity in an experiment can be relatively difficult. To this end, the Clauser chart method (Clauser, 1954) is used to estimate u_τ . By sketching U^+ versus z^+ (where $z^+ = zu_\tau/\nu$) on a semi-logarithmic scale along the x -axis, the overlap region of the boundary layer is denoted as a straight line. This region is subsequent to the log law given by

$$\frac{U(z)}{u_\tau} = \frac{1}{\kappa} \log \left(\frac{zu_\tau}{\nu} \right) + B, \quad (6)$$

where $\kappa = 0.41$ is the von Kármán constant $B = 5$ is the constant used in Clauser (1954). The presence of the logarithmic region in an adverse pressure gradient boundary layer is still under discussion (Monty, Harun and Marusic, 2011), but it is known that a turbulent boundary under the effect of an adverse pressure-gradient evolves towards the zero-pressure-gradient state. Monty et al. (2011) pointed out that the skin friction, estimated from the Clauser chart

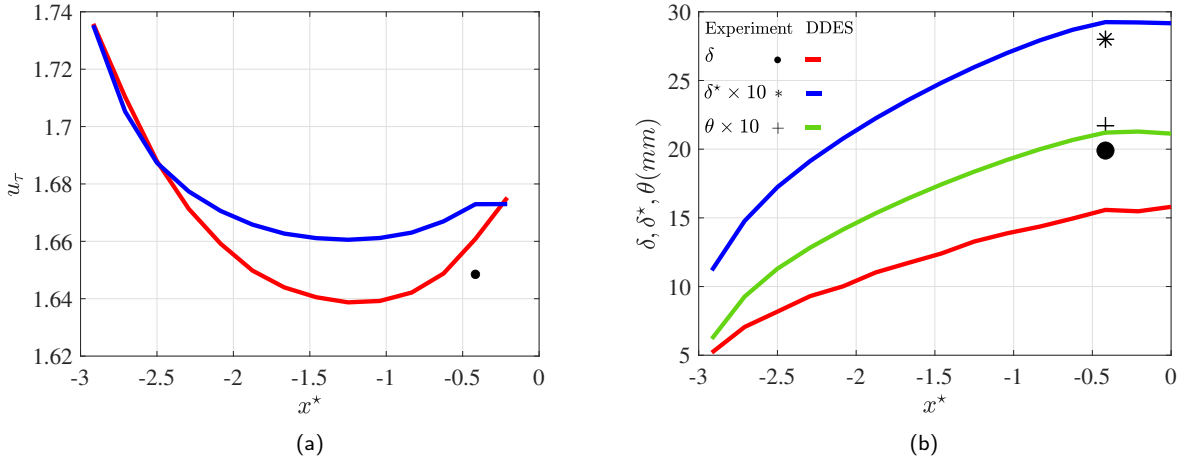


Figure 6: (a) Evolution of the friction velocity, u_τ along the roof of the body at $y = 0$, black dots represent experimental data. Red represents the DDES while blue reports results from RANS. (b) Streamwise evolution of the boundary-layer characteristic thicknesses δ , δ^* and θ .

method is matched with that determined from oil-interferometry for smooth adverse pressure gradient, at $Re_\theta = 11860$. In fact, for mild pressure gradients, that is when $\beta < 3$, the skin friction obtained using both methods was satisfactory. However, for $\beta > 3$, the difference between both approaches becomes significant, with up to 10% variation in C_f . In equation (6), $U(z)$ can be estimated directly from the experiments assuming that ν , κ , and B are constants. Thus, the only unknown term is u_τ . Besides that, figure 5b shows the normalized boundary layer by u_τ and z^+ , and the different regions associated to the viscous sub-layer $z^+ < 5$, the buffer layer $5 < z^+ < 30$, the turbulent region $30 < z^+ < 300$, and the outer region. All profiles show a fairly good agreement between the simulation (for both models) and the experiment. Note that DDES performs yet better than RANS as shown in figure 5b, both in terms of thickness and mean velocity. Figure 6a shows the evolution of u_τ , calculated by the simulation and compared to that estimated using the Clauser method. Consequently, 15 points were extracted from the simulation data, covering locations along x^* in the range $[-3, 0]$ across the top of the body surface. Figure 6b reports the growth of δ , δ^* and θ along the x -direction, where the integral parameters (δ^* , θ) also increase until they reach their maximum value at $x = -0.4H$, remaining constant until the body's end.

5.2. Global aerodynamic quantities

Aerodynamics coefficients such as the drag coefficient C_d are key factors to diagnose the performances of road vehicles but they can be particularly difficult to measure in full-scale applications. There is a clear need for key performances indicators that can be upscaled to full-scale models. In fact, C_d is known to be linked to other flow parameters, such as the recirculation region length and the base pressure drag. For this purpose, we introduced a summarised comparison between experimental and simulation results in this section and further carry on the analysis in the next subsection.

The drag coefficients is given by

$$C_d = \frac{2D}{\rho S U_\infty^2}, \quad (7)$$

where D is the drag force and S is the projected model frontal area ($S = 0.112 \text{ m}^2$). The pressure coefficient writes

$$C_p = 2 \frac{p - p_\infty}{\rho U_\infty^2}, \quad (8)$$

where p_∞ is the free-stream static pressure. The base drag was estimated by integrating the pressure coefficient as

$$C_{db} = \frac{1}{S_b} \oint_{S_b} \bar{C}_p dS, \quad (9)$$

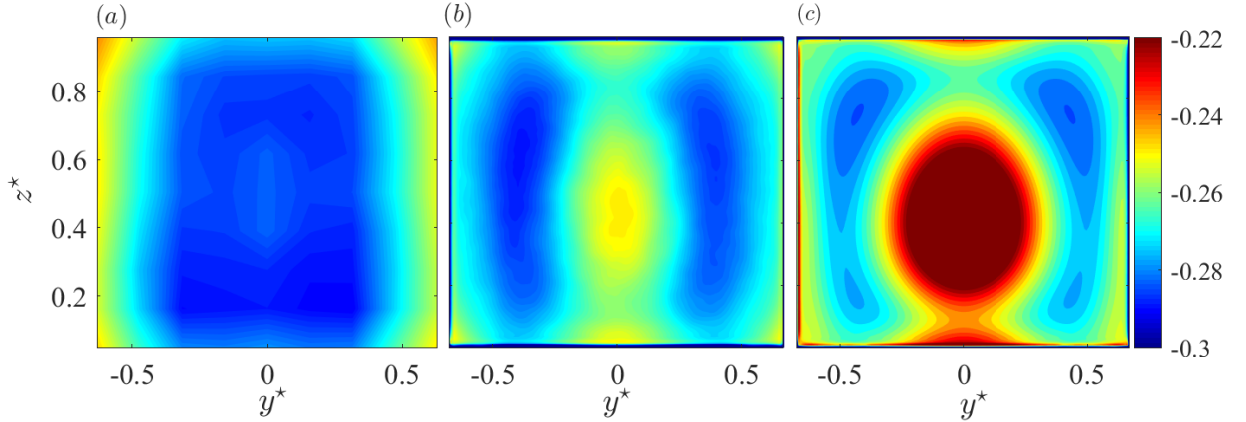


Figure 7: Pressure distribution $\bar{C}_p^*(x = 0, y^*, z^*)$ for (a) experiment, (b) DDES, and (c) $k - \omega$ SST measured at the base of the body.

	C_d	$\Delta C_d \%$	C_{db}	$\Delta C_{db} \%$	l_r^*	$\Delta l_r \%$
<i>Exp.</i>	0.333	0	-0.273	0	1.57	0
<i>DDES</i>	0.326	2%	-0.256	6%	1.67	7%
<i>k - ω SST</i>	0.31	7%	-0.249	9%	2.04	30%

Table 2

Table of drag coefficient C_d , base-pressure drag coefficient (\bar{C}_{pb}) and normalised recirculation region length $l_r^* = l_r/H$.

where \bar{C}_p is the time average estimated base-pressure coefficient while S_b is the area covered by the pressure taps. Mean base-pressure distributions $\bar{C}_p(x^* = 0, y^*, z^*)$ are shown in figure 7. Experimental results are comparable to the results of Volpe et al. (2015) and Grandemange et al. (2013c) but several differences can be noted with both numerical simulations. Pressure recovery is in better agreement with the DDES than RANS but both simulations overestimate the pressure at the centre of the base. Note that the pressure coefficient calculated near the edges, where the boundary layer ends, are in relatively good agreement, hinting to the role of the wake in these discrepancies. The mean pressure coefficient at the base C_{db} in the experiment is in relatively good agreement with the DDES (6% difference) but begins to deviate for the $k - \omega$ SST (9% difference) (see table 2).

The mean recirculation region is shown in figure 8, measured at the transverse mid plane and for each of the three methods. While experiments compare favourably with the mean recirculation region obtained from the DDES, the RANS approach is a far fetch. The recirculation length is defined by the mean separation line (defined by the isovalue $U(x, y) = 0$), such that $l_r = \max(x|_{U^*=0})$, at the tip of the recirculation region. In table 2, $\Delta l_r = (l_r^{sim.} - l_r^{exp.})/l_r^{exp.}$ is computed as the difference between the simulation and the experiment. From these results, it is clear that the recirculation length predicted with the RANS approach is 30% larger than the experiment. Instead, only 7% separate the results between the DDES and the experiment. Note that the isosurface defined by $U(x_r) = 0$ will be used later in order to understand where the discrepancies between the model and the experiment come from.

The differences between RANS and DDES carry similarly for the base pressure coefficient and the drag coefficient. RANS under estimates the drag coefficient by 7% and the base-pressure coefficient by 9% compared to the experiment. At the contrary, DDES is only 2% away from experimental measurements while the base pressure reaches 6% error. Clearly, a such discrepancy cannot come from the boundary layer itself since it was found to be nearly equivalent between RANS and DDES. The streamlines of the mean flow are shown in figure 8(a,c,e) where the recirculation region differs essentially at the bottom shear layer. In the RANS case, the flow near the end of the recirculation region shows a surprisingly large amount of negative vertical velocity. This in turn produces a weaker horizontal pressure gradient as shown in figure 8(f) for the RANS case, compared to the experiment and the DDES case (cf. figures 8(b,d)). An analysis will be carried out in the region to understand how the bottom shear layer interacts with the ground and the upper shear layer.

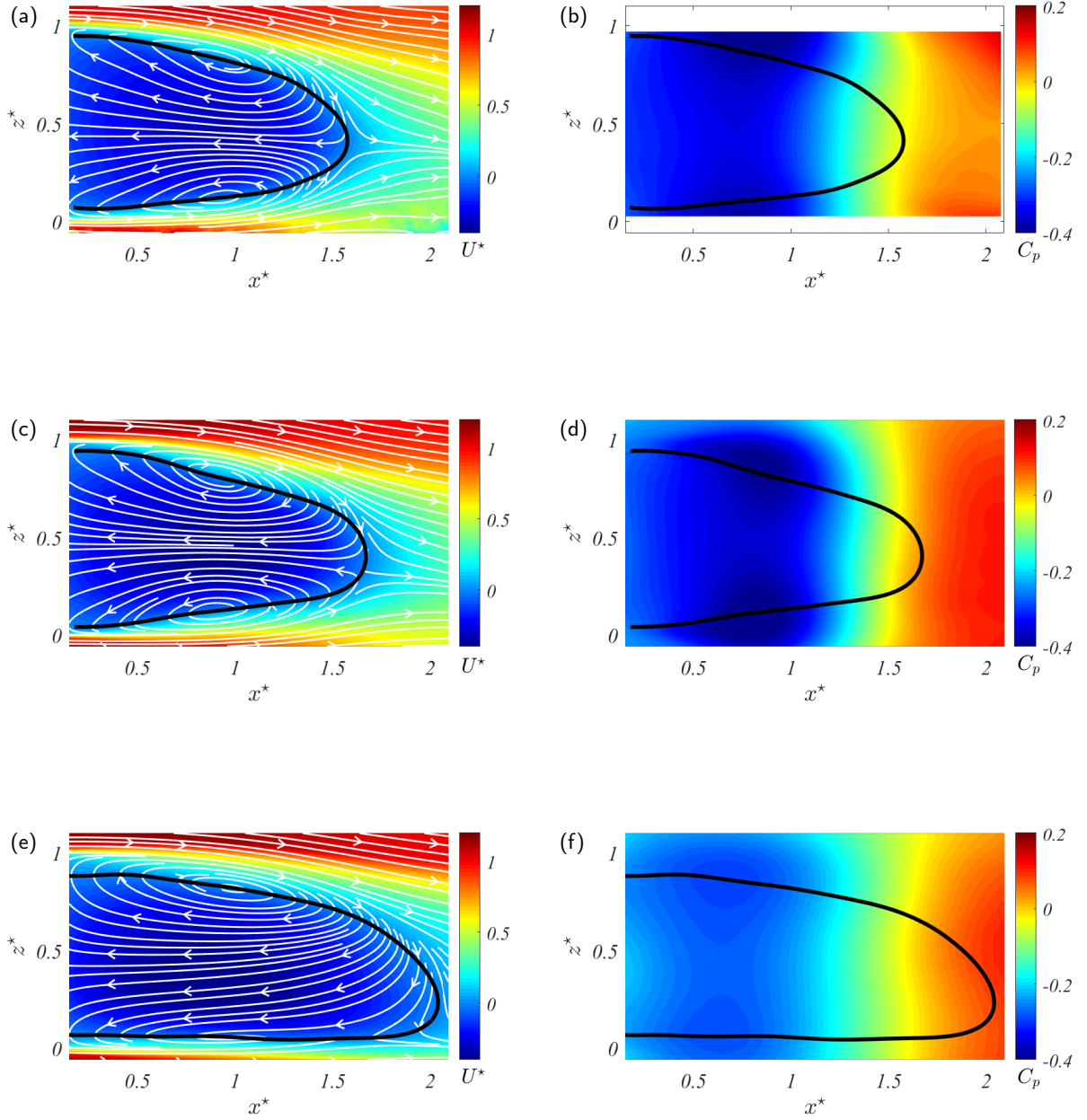


Figure 8: Time-averaged horizontal velocity and pressure coefficient contours along the $x - z$ -plane at $y = 0$ for (a,b) experiments, (c,d) DDES, and (e,f) $k - \omega$ SST.

5.3. Wake topology

The Recirculation Region Interface (RRI), defined as the zero-horizontal velocity surface, such that

$$RRI(x_i) = (x_i) \Big|_{U(x_i)=0}, \quad (10)$$

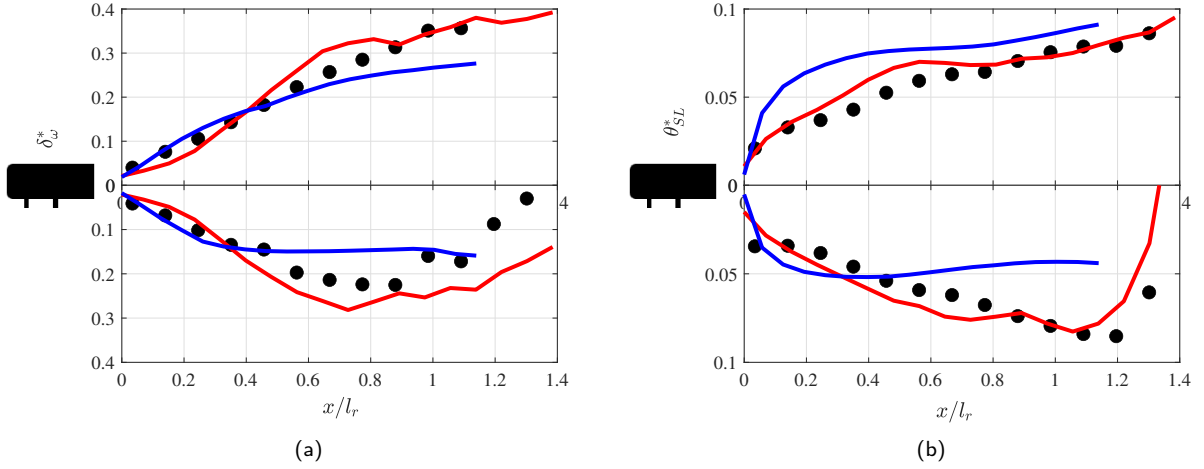


Figure 9: (a) Vorticity thickness (δ_ω) normalized by the height of the body against the streamwise direction x normalized by the recirculation length l_r for the upper and lower part. **(b)** Momentum thickness (θ_{SL}) normalized by the height of the body for the upper and lower part. The DDES is shown in red, the RANS in blue, and the experiment by means of symbols.

is the three-dimensional mean separation line shown using a continuous black line in the two-dimensional plane in figure 8, and bounds the mass exchanges between the recirculation region and the outer flow. The RRI is a useful tool as it provides both a systematic geometric tool to measure, for instance, the recirculation length, or integrate the momentum equation to derive an equation relating the aerodynamic drag to the flow quantities in a budget.

The streamlines depicted in figure 8 show that the RRI passes through the centre of the vortex of the mean wake and therefore accounts for the mean mass entrained within the wake (Stella, Mazellier, Joseph and Kourta, 2018). The vortex-centre top location for the experiment and DDES model, along the upper shear layer is located at $x^*=0.9$ and $z^*=0.82$, while it is located at $x^*=0.9$ and $z^*=0.15$ for the lower shear layer. In contrast, the RANS simulation gives a distinct location, at $z^*=0$ for the lower shear layer and $z^*=0.87$ for the upper one both at $x^*=1$. This inconsistency in vortex location and dimension has a direct effect on the shape of the recirculation region, which can be clearly observed in figure 8 and thereby impacts the mass entrained together with drag.

5.4. Shear-layer growth

As illustrated in figure 1, the RRI delimits the inner boundary of the shear layer and the respective development of both the upper and lower shear layers have to be related.

The separated shear-layer development is analysed based on the vorticity thickness δ_ω , and momentum thickness θ_{SL} . Following Dandois, Garnier and Sagaut (2007), δ_ω and θ_{SL} are computed as follows

$$\delta_\omega = \frac{U_{max}(x) - U_{min}(x)}{(\partial U(x, z)/\partial z)_{max}}, \quad (11)$$

and

$$\theta_{SL} = \int_0^\infty \left(\frac{U(x, z) - U_{min}(x)}{(U_{max}(x) - U_{min}(x))} \right) \left(1 - \frac{U(x, z) - U_{min}(x)}{(U_{max}(x) - U_{min}(x))} \right) dz, \quad (12)$$

where $U_{min}(x)$ and $U_{max}(x)$ are the minimum, and maximum velocities respectively, along the streamwise direction. The shear layer is further divided into two parts (i.e. upper and lower) reconnecting at $x = l_r$. The shear-layer thicknesses linearly increase until a value of $x/l_r \approx 0.8$ for both, the experiment and DDES. For the RANS case, this growth stops near $x/l_r = 0.4$. Bonnet, Delville, Glauser, Antonia, Bisset, Cole, Fiedler, Garem, Hilberg, Jeong, Kevlahan, Ukeiley and Vincendeau (1998) suggest that the growth rate of the shear layer scales as

$$\frac{\delta_\omega}{x} = 0.17R \quad \text{where} \quad R = \frac{U_\infty - U_{min}}{U_\infty + U_{min}}. \quad (13)$$

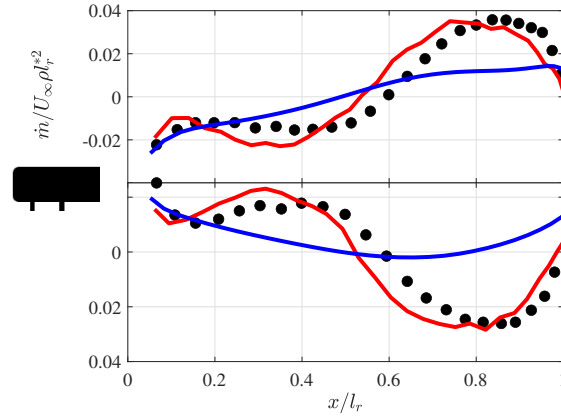


Figure 10: Mass entrainment comparison along the RRI where the DDES is shown in red, the RANS in blue, and the experiment by means of symbols.

According to equation (13), $d\delta_\omega/dx$ should be approximately equal to 0.2–0.23. In our case, the slope is approximately 0.34 near the body and 0.25 over the full extent of the near wake, which is in agreement with values expected for a free mixing layer, as reported for two-dimensional mixing layers (Brown and Roshko (1974)) or the curved mixing layers (Tenaud, Fraigneau et al. (2011)).

Figure 9b shows the growth of the momentum thickness θ_{SL} . The behaviour of θ_{SL} is similar to δ_ω but with a slope of 0.047. In their experiment of free mixing layers, Browand and Troutt (1985) reported that the growth rate of the momentum thickness is well predicted by

$$\frac{\theta_{SL}}{x} = 0.034R. \quad (14)$$

In reference to equation (14), $d\theta_{SL}/dx$ should be equivalent to 0.041–0.046 which is consistent with the value of 0.047 expected for a free mixing layer. In addition, the rate of shear-layer growth $\delta_\omega/\theta_{SL}$ is 4.6 for $x/l_r = 1$ which is also consistent with the observations of a 2D mixing layer (Bonnet et al., 1998) where $\delta_\omega/\theta_{SL} \approx 4.8$ was found. The growth of $\delta_\omega/\theta_{SL}$ is 5.6 for $x/l_r = 1$. With respect to their mixing layers, Castro and Haque (1987) and Larchevêque, Sagaut, Lê and Comte (2004) observed that the ratio between the growth rates of the momentum and vorticity thicknesses has a value close to 5, which is comparable with that noticed in the present study at the lower part of the wake. Note that the symmetry between the upper and lower shear layer in the experiment can be explained by the rather large value of the ground clearance which has little effect for the present setup (see Grandemange et al. (2013c) for a detailed study on ground clearance effects).

The shear-layer growth reported for the experiment is in fairly good agreement with those observed from the DDES model, as shown in figure 9. At the contrary, RANS behaves differently. Indeed, both δ_ω and θ_{SL} are characterised by a lower shear-layer growth rate, where the ground proximity considerably impacts the shear-layer development. The separated shear layers act similarly to a free-shear layer, and their growth are dominated by the entrainment in the large region downstream Ahmed body model. However, this would have significant importance for the present study because the spreading of the free-shear layers is driven by the entrainment of external fluid Pope (2001). In order to shed light on the sources of differences between DDES/experiments and RANS simulations, we turn to the analysis of the mass entrained into the wake to complement the results obtained from the shear-layer analysis.

5.5. Mass entrainment

Since the shear-layer growth drives the aerodynamic properties in the near wake, the mass transfer across the boundaries of the shear layer set the topology of the wake, and the RRI is used to diagnose the mass exchanges between the recirculation region and the outer flow. This topic is of fundamental importance for understanding and controlling the near wake because of two reasons. First, several studies have shown that one of the driving mechanisms of the near wake is the dynamic balance between the back flow and the amount of fluid that reenters the wake through the shear layer in the region of separation (Stella et al., 2017; Lorite-Diez, Jimenez-Gonzalez, Pastur, Martinez-Bazan and Cadot,

	Exp.	DDES	$k - \omega$ SST
$\dot{m}_{in_{top}}^*$	0.05	0.06	0.05
$\dot{m}_{in_{bot}}^*$	0.03	0.04	0.008
$\dot{m}_{out_{top}}^*$	-0.03	-0.03	-0.05
$\dot{m}_{out_{bot}}^*$	-0.03	-0.03	-0.04
$\frac{ \dot{m}_{bot}^* }{ \dot{m}_{top}^* }$	75%	75%	48%

Table 3

Mass flux integrated along the RRI interface (normalized by $\rho H U_\infty$).

2020). Second, the results presented in §5.4 have shown that the size of the recirculation region is directly related to the growth rate of the shear layer. Gerrard (1966) proposed a mechanism, which is the result of the equilibrium of a mass flux entering and leaving the recirculation region which sets the recirculation length. For the present case, the growth rate of the free-shear layers is associated with velocity entrainment along the shear layer. Therefore, it seems necessary to tie a link between shear-layer growth and the mass balance equation through the RRI which precisely follows the shear layer. The same principle of mass entrainment and recovery, between the shear and the recirculation regions, is expressed by Mair (1978) for two-dimensional bluff bodies as

$$\dot{m}^* = - \int_{l_{RRI}} W^*(l^*) \cos(\phi(l^*)) dl^* = - \int_{l_{RRI}} W^*(x^*) dx^* \quad (15)$$

where \dot{m}^* is the mean mass flux, l_{RRI} is the RRI boundary length, and ϕ is the angle between the normal of the surface and the z -axis; while, l^* is the curvilinear abscissa at the RRI. In what follows, we only study a two-dimensional RRI obtained in the midplane at $y^* = 0$ for consistency with the experiment.

The evolution of the mass flux in the longitudinal direction, along the RRI, is shown in figure 10 where the mass flux is approximately symmetric. Therefore, the mass transfer according to its positive/negative values, can be separately studied. Table 3 reflects the integration of the mass entrained along the first range (negative mass flux), denoted by $\dot{m}_{out_{top}}^*$ and $\dot{m}_{out_{bot}}^*$, for the upper and lower parts of the RRI respectively. While the integration of the mass flux over the second range (positive mass flux); that is termed $\dot{m}_{in_{top}}^*$ and $\dot{m}_{in_{bot}}^*$, for the upper and lower sides of the RRI interface. Thus, the first interesting point that is reported in Table 3, is the symmetric behaviour between the upper and lower parts of the RRI interface for the experiment and DDES model. In contrast, RANS results are different. The entrainment feeding the recirculation comes from the upper part of the interface and explains the asymmetry of the recirculation bubble.

Shear-layer and the mass-entrainment analyses show that the comparison between experiments and DDES holds fairly well but the RANS turbulence model clearly under predicts the entrainment at the bottom shear layer. In the following section, this comparison will be completed by linking this effect to the total drag. As shown in table 2, more than 80% of the drag comes from the base drag. In other words, to describe how the near wake interacts and affects the recirculation region topology, it is necessary to understand what drives the base pressure and therefore drag changes. The RANS recirculation presents a higher aspect ratio l_r^* , distinct from the DDES and the experiment where an increase of entrainment decreases l_r^* . This scenario is consistent with Roshko's models on the wake equilibrium and base pressure (Roshko, 1955, 1993a,b) as well as more recently reported in Barros, Borée, Noack, Spohn and Ruiz (2016). Next, we analyse the momentum budget to link the shape of the near wake to the drag through the RRI.

5.6. Momentum budget

In an analogy to the simplified two-dimensional wake, the streamwise mean momentum balance, through the closing separating line (i.e. the DSI) of the recirculation region was reevaluated by Balachandar, Mittal and Najjar (1997) who showed that the base pressure coefficient is linked to the pressure, normal, and shear stresses along the DSI interface. However, the main issue in this study is that the unavailable pressure downstream the body, in the experiments, is impacting this discussion. To circumvent this issue, we will use the pressure estimation method recently proposed by Shanmughan et al. (2020) and use the RRI for the analysis instead.

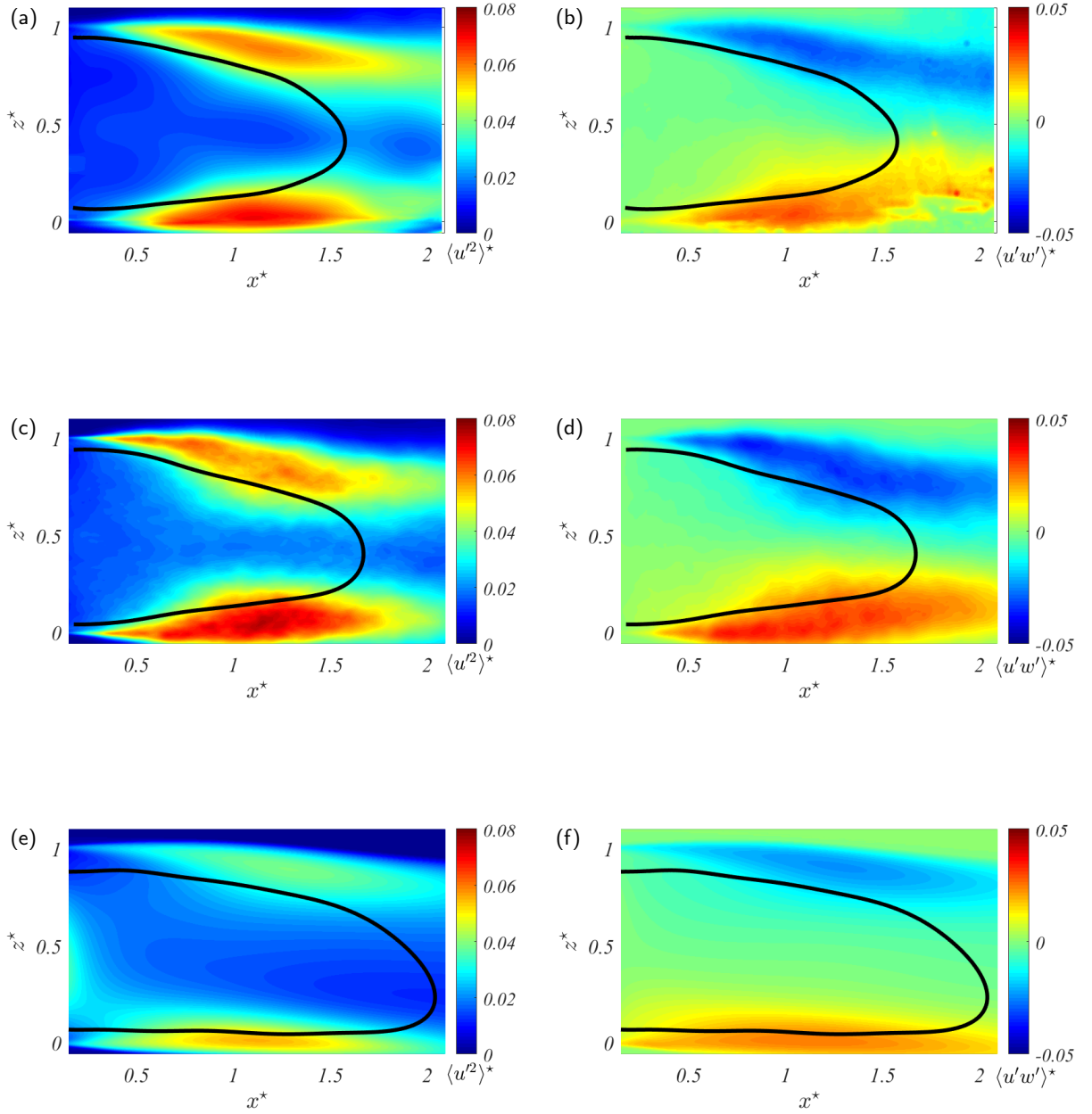


Figure 11: Time-averaged turbulent horizontal normal stress and shear stress contours along the $x - z$ -plane at $y = 0$ for (a,b) experiments, (c,d) DDES, and (e,f) $k - \omega$ SST.

We now proceed with the analysis of the turbulent Reynolds stresses which are shown in figure 11 for the experiment and both numerical simulations in the mid plane of the wake. In order to compute the momentum budget, the RRI line is divided it into two parts; the upper part and the lower part as shown in figure 1. Figures (12c and 12d) show the turbulent normal- and shear-stress terms normalised by U_∞^2 along the upper part of the RRI line. In figure 12c, we noticed that the increase of $\langle u'^2 \rangle^*$ along the RRI is similar between experiment and the DDES, values increase until $x/l_r = 0.8$

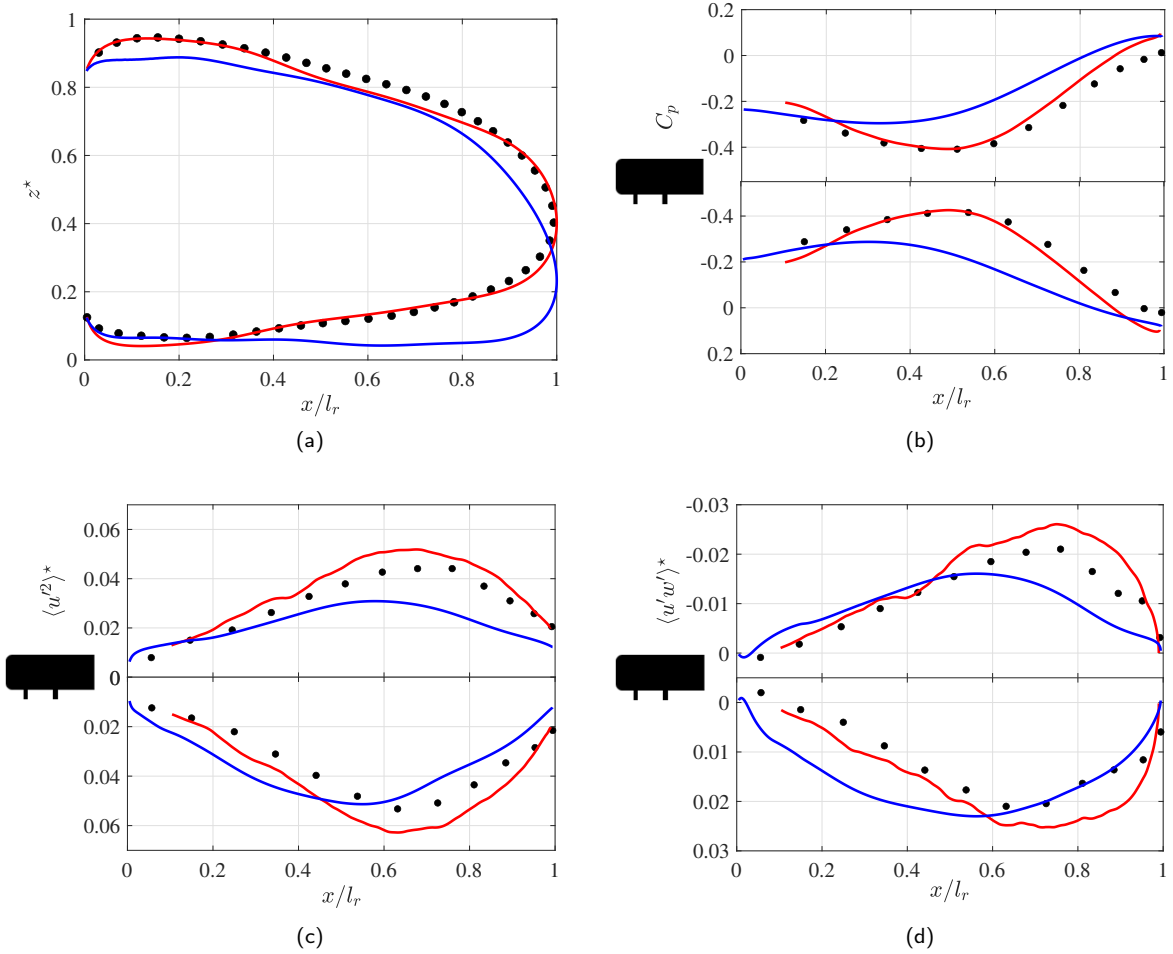


Figure 12: (a) Recirculation region interface. (b) pressure projected along the RRI, (c) normal stress, $\langle u'^2 \rangle^*$ along the upper part of the RRI interface. (d) Shear stress, $\langle u'w' \rangle^*$ along the upper part of the RRI interface. The DDES is shown in red, the RANS in blue, and the experiment by means of symbols.

to reach a maximum $\langle u'^2 \rangle^* = 0.04$, then decreases until $\langle u'^2 \rangle^* = 0.02$ at $x/l_r = 1$. In figure 12d, the decreasing $\langle u'w' \rangle^*$ along the RRI is similar between experiment and DDES. The shear stresses decreases until $x/l_r = 0.8$ to reach a minimum $\langle u'w' \rangle^* = -0.02$, then it increases until it reaches $\langle u'w' \rangle^* = 0$ at $x/l_r = 1$. These results show that the normal and shear stresses play an important role in the $0.5 < x/l_r < 1$ region. Figures also show the different order of magnitude of the shear stress so that $\max(\langle u'w' \rangle^*)$ is half the maximum of $(\langle u'^2 \rangle^*)$. The difference between DDES/experiments and RANS simulations clearly arises from the turbulent stresses which are fully modelled using an eddy-viscosity assumption for the RANS case.

For two-dimensional bluff body flows, the streamwise momentum balance on the RRI line writes

$$C_{pb} = \int_{RRI^-} \kappa \left(C_p + 2\langle u'^2 \rangle^* \right) - 2\langle u'w' \rangle^* dx^* - \int_{RRI^+} \kappa \left(C_p + 2\langle u'^2 \rangle^* \right) - 2\langle u'w' \rangle^* dx^*, \quad (16)$$

where C_{pb} represents the body-base pressure, C_p is the pressure distribution along the RRI line in addition to normal and shear components. In what follows, each term and their contribution in the budget along the upper and lower part of the RRI is analysed and compared with the experiment through a cumulative integral analysis of equation (16) along the x direction. Figure 13b shows that the pressure term is shown along with the upper (blue) and lower (red) part of the RRI line for the DDES model where two regions appear. The first one is from $0 < x/l_r < 0.41$, in this region, the pressure terms for both parts are symmetric and provide a negative contribution to the drag (an actual net thrust)

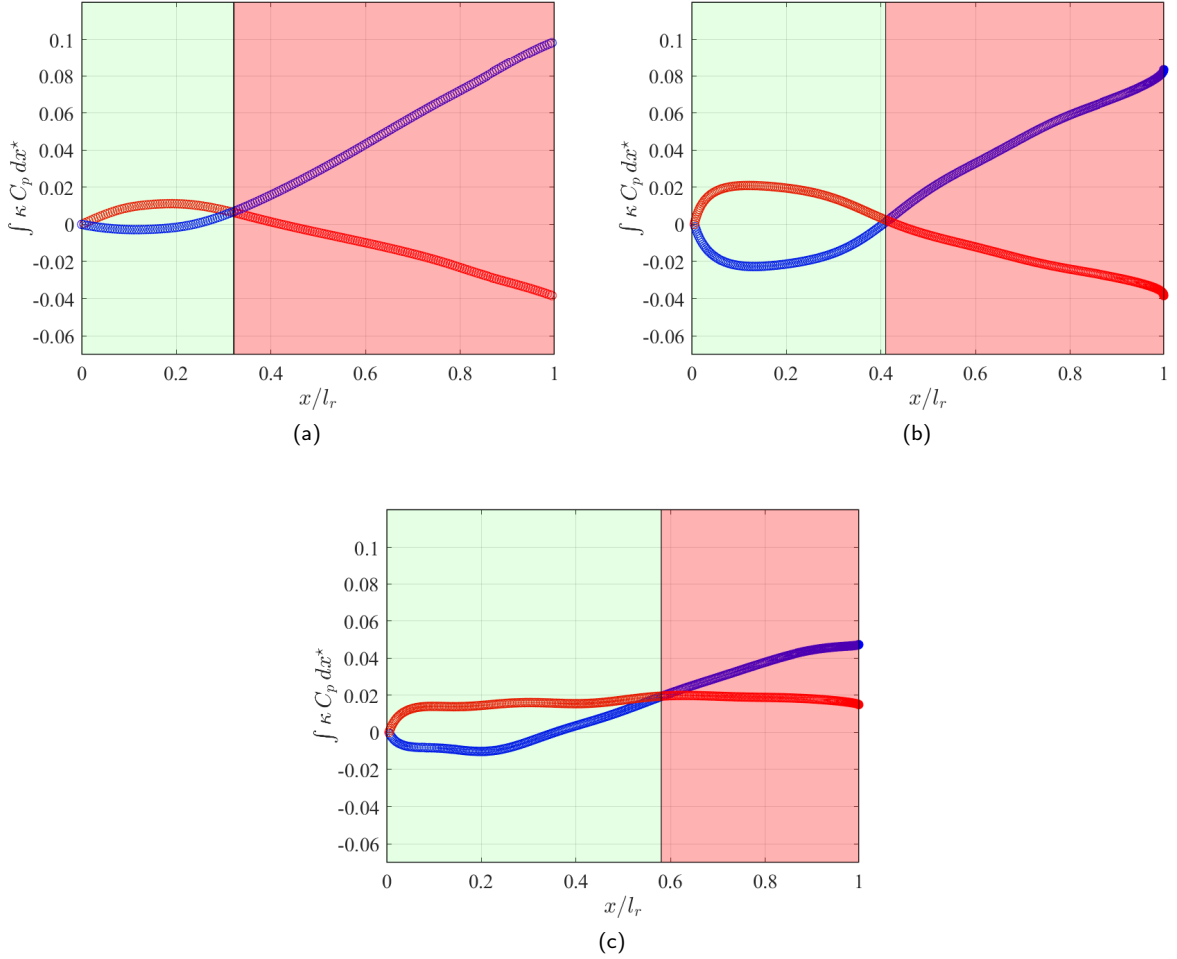


Figure 13: Cumulative integral of the pressure term along the upper and lower part of the RRI interface for (a) experiment, (b) DDES, (c) $k - \omega$ SST. Blue symbols show the upper part while red symbols show cumulative integral on the lower part of the RRI.

(Red-Blue>0). The second region starts from $0.41 < x/l_r < 1$, here we notice that the symmetry between the upper and lower part is broken, and the pressure term starts to play a role in increasing the pressure base. Figure 13c, the pressure term is shown along with the upper and lower part as well, for the $k - \omega$ SST model. Two regions can be again identified. The first one is from $0 < x/l_r < 0.59$ where in this region, the pressure term for the two parts is asymmetric and provide a negative contribution to the drag (Red-Blue>0). The second region starts from $0.59 < x/l_r < 1$, where the pressure term starts to play a role in increasing the pressure base. The physics between the SST $k - \omega$ and DDES is completely different, and the $k - \omega$ SST shows a region of thrust for the lower part of the RRI while a region of drag in the upper RRI. Experimental results are reported in figure 13a and compare favorably with the DDES. Note that for $x = l_r$, the pressure contribution for the experiment falls very close to that obtained in the DDES and demonstrates the robustness of the pressure reconstruction algorithm (Shanmughan et al., 2020).

In figure 14(a,c), the cumulative integral along the streamwise direction of the normal stress term is shown along with the upper (blue) and lower (red) part of the RRI line for the experiment and the DDES model respectively. The first region here is from $0 < x/l_r < 0.31$, in this region, the normal stress term for the two parts are symmetric and increase the pressure base (Red-Blue<0). The second region starts from $0.31 < x/l_r < 1$, here we noticed that the symmetry between the upper and lower part is broken too, and the normal stress term starts to play a role in decreasing

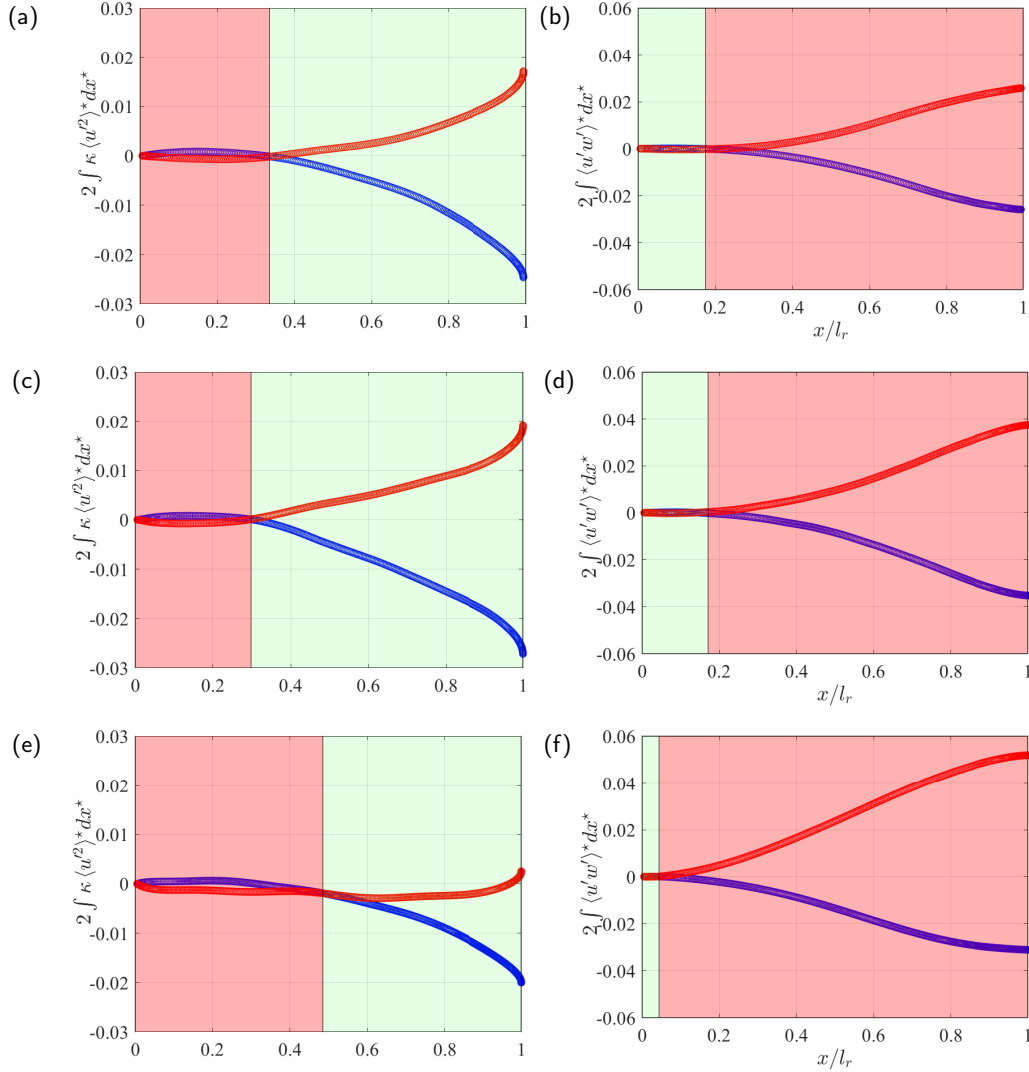


Figure 14: Normal stress term along the upper and lower part of RRI interface for (a) experiment, (c) DDES, (d) $k - \omega$ SST (blue:upper, red:lower). Shear stress term along the upper and lower part of RRI interface for (b) experiment, (d) DDES, (f) $k - \omega$ SST.

the pressure base. In figure 14(e), the normal stress term is shown along with the upper and lower part as well, for the SST $k - \omega$ model. The first region is from $0 < x/l_r < 0.5$, in this region, the normal stress term for the two parts are asymmetric and play a helper role (Red-Blue>0). The second region starts from $0.5 < x/l_r < 1$, here we noticed that this term starts to play a role in decreasing the pressure base. The physics between the experiment and DDES is the same, while both with SST $k - \omega$ are completely different.

In figure 14(b) and 14(d), the shear stress term is shown along with the upper and lower part of the RRI line for the experiment and DDES model. The first region here is from $0 < x/l_r < 0.185$ where the shear stress terms for the two parts are symmetric and decrease the base pressure (Red-Blue<0). The second region starts from $0.185 < x/l_r < 1$. Here we notice that the symmetry between the upper and lower part is still present, while the shear-stress term starts to play a role in increasing the pressure base. In figure 14(f), the shear stress term is shown along with the upper and lower part, for the $k - \omega$ model SST. The first region is from $0 < x/l_r < 0.05$, in this region, the shear stress terms on each side of the RRI are asymmetric and decrease the drag (Red-Blue>0). The second region starts from $0.05 < x/l_r < 1$ where shear stress term starts to play a role in increasing the pressure base. The physics between the experiment and DDES

remain the same, while the $k - \omega$ SST over predicts the shear stresses while under predicting the normal stresses. It comes clear that the eddy-viscosity assumption is unable to accurately predict the turbulent stresses, leading to a deficit in mass entrainment through the bottom boundary layer, leading to the asymmetry of the wake in the RANS simulation and the over extent of the recirculation region.

6. Conclusions

The present study analyses the time-averaged wake properties of an Ahmed body at high Reynolds numbers comparing mean results from experiments and simulations at $Re_H = 7.7 \times 10^5$. Two different turbulence models are analysed and compared with experimental results using mass and momentum budgets performed along the recirculation region interface for the vertical plane positioned at the centre of the wake. Boundary-layer characteristics, shear-layer growth, and the near-wake mass and momentum budgets allow for quantifying the role of each part of the flow in driving drag. A comparison of the drag coefficients and characteristic length scales of the wake between the experiment and the delayed detached eddy simulation confirm a good agreement.

The shear-layer growth appears to follow the same scaling laws than previously observed for free-shear layers, and this, for both numerical simulations and the experiment, thereby preventing any definitive conclusions regarding a quantitative comparison. The analysis is then reconsidered in the framework of a mass and momentum budget along the recirculation region interface which allows for accessing both the mass entrained through the recirculation region (respectively detrained outside). This simple, yet effective analysis highlights that for RANS simulations, the amount of mass entrained by the bottom shear layer is clearly under predicted by a factor 4 when compared with the experiment. Then, the momentum budget along the recirculation interface allows for linking turbulent stresses with the pressure inside the recirculation region and the base of the body. To do so, the pressure reconstruction technique recently proposed by Shanmughan et al. (2020) is used to compute the mean pressure in the wake from experimental data and shows an excellent agreement with the DDES in the mid plane although the flow is essentially symmetric yet three-dimensional. The momentum budget highlights that turbulent stresses are systematically under predicted in the RANS simulation and asymmetric, which is symptomatic of the calibration of the eddy viscosity. Whence, under predicting both the normal and shear stresses leads to the mass entrainment deficit reported in the mass budget. This in turn alters the growth of the shear layers, and thus, the pressure at the base predicted by the RANS simulation, leading to an unrealistic downwash of the recirculation region.

On the other hand, the delayed detached eddy simulation captures the same physical behaviour than the experiment and the contributions to the momentum budget all compare favourably with the experiment. Both the geometry of the near wake and the contribution of the different terms in the base-drag budget follow nearly identical trends. Overall, the recirculation region interface can be sought as a generic mean to decompose and diagnose drag in bluff-body wakes and understand the momentum balance in complex three-dimensional flows.

The tools developed in this study naturally extend to three-dimensional wakes as well as more realistic geometries. This particular aspect is currently under investigation in our group in the case of an Ahmed body and a realistic car geometry, representing interesting test cases to understand, model, and control the physical phenomena at the origin of drag for road vehicles.

Acknowledgement:

This work was supported by the French National Research Agency (ANR) through the COWAVE Project (ANR-17-CE22-0008-01). This work was granted access to the HPC resources of CINES/IDRIS under the allocations 2019-2a0129 and 2020-2a0129 made by GENCI.

References

- Ahmed, S., Ramm, G., Faltin, G., 1984. Some salient features of the time-averaged ground vehicle wake, in: SAE Technical Paper, SAE International. URL: <https://doi.org/10.4271/840300>, doi:10.4271/840300.
- Balachandar, S., Mittal, R., Najjar, F., 1997. Properties of the mean recirculation region in the wakes of two-dimensional bluff bodies. *Journal of Fluid Mechanics* 351, 167–199.
- Barros, D., Borée, J., Noack, B.R., Spohn, A., Ruiz, T., 2016. Bluff body drag manipulation using pulsed jets and coanda effect. *Journal of Fluid Mechanics* 805, 422–459. doi:10.1017/jfm.2016.508.
- Beaudoin, J., Cadot, O., Ji, A., Gosse, K., Paranthoen, P., Hamelin, B., Tissier, M., Allano, D., Mutabazi, I., Gonzales, M., Je, W., 2004. Cavitation as a complementary tool for automotive aerodynamics. *Experiments in Fluids* 37, 763. URL: <https://hal.archives-ouvertes.fr/hal-00017106>.

- Bonnet, J., Delville, J., Glauser, M., Antonia, R., Bisset, D., Cole, D., Fiedler, H., Garem, J., Hilberg, D., Jeong, J., Kevlahan, N., Ukeiley, L., Vincendeau, E., 1998. Collaborative testing of eddy structure identification methods in free turbulent shear flows. *Experiments in Fluids* 25, 197–225. doi:10.1007/s003480050224.
- Browand, F., Troutt, T., 1985. The turbulent mixing layer: geometry of large vortices. *Journal of Fluid Mechanics* 158, 489–509.
- Brown, G.L., Roshko, A., 1974. On density effects and large structure in turbulent mixing layers. *J. Fluid Mech.* 64, 775–816.
- Castro, I., Haque, A., 1987. The structure of a turbulent shear layer bounding a separation region. *Journal of Fluid Mechanics* 179, 439–468.
- Clauser, F.H., 1954. Turbulent boundary layers in adverse pressure gradients. *Journal of the Aeronautical Sciences* 21, 91–108. URL: <https://doi.org/10.2514/8.2938>, doi:10.2514/8.2938, arXiv:<https://doi.org/10.2514/8.2938>.
- Conan, B., Anthoine, J., Philippe, P., 2011. Experimental aerodynamic study of a car-type bluff body. *Experiments in Fluids* 20, 1273–1284. URL: <https://hal.archives-ouvertes.fr/hal-01319500>, doi:10.1007/s00348-010-0992-z.
- Dalla Longa, L., Evstafyeva, O., Morgans, A.S., 2019. Simulations of the bi-modal wake past three-dimensional blunt bluff bodies. *J. Fluid Mech.* 866, 791–809.
- Dandois, J., Garnier, E., Sagaut, P., 2007. Numerical simulation of active separation control by a synthetic jet. *Journal of Fluid Mechanics* 574, 25–58. doi:10.1017/S0022112006003995.
- Evstafyeva, O., Morgans, A.S., Dalla Longa, L., 2017. Simulation and feedback control of the ahmed body flow exhibiting symmetry breaking behaviour. *Journal of Fluid Mechanics* 817, R2. doi:10.1017/jfm.2017.118.
- Gerrard, J., 1966. The mechanics of the formation region of vortices behind bluff bodies. *Journal of fluid mechanics* 25, 401–413.
- Grandemange, M., Gohlke, M., Cadot, O., 2013c. Bi-stability in the turbulent wake past parallelepiped bodies with various aspect ratios and wall effects. *Physics of Fluids* 25, 5103. doi:10.1063/1.4820372.
- Gritskevich, M.S., Garbaruk, A.V., Schütze, J., Menter, F.R., 2012. Development of DDES and IDDES Formulations for the $k-\omega$ Shear Stress Transport Model. *Flow, Turbulence and Combustion* 88, 431–449.
- Guilmineau, E., B., D.G., Leroyer, A., Queutey, P., Visonneau, M., Wackers, J., 2018. Assessment of hybrid rans-les formulations for flow simulation around the ahmed body. *Comput. & Fluids* 176, 302–319.
- Guilmineau, E., Deng, G., Quentey, P., Visonneau, M., 2016. Assessment of turbulence models for flow simulation around the ahmed body, in: 11th International ERCOFTAC Symposium on Engineering Turbulence Modelling and Measurements - ETMM11, Palermo, Italy. URL: <https://hal.archives-ouvertes.fr/hal-02570941>.
- Harker, M., O’Leary, P., 2008. Least squares surface reconstruction from measured gradient fields, in: 2008 IEEE conf. Comput. Vision & Patt. Recog., IEEE. pp. 1–7.
- Harker, M., O’Leary, P., 2013. Direct regularized surface reconstruction from gradients for industrial photometric stereo. *Comput. Indus.* 64, 1221–1228.
- Hesse, F., Morgans, A.S., 2021. Simulation of wake bimodality behind squareback bluff-bodies using les. *Comput. & Fluids* 223, 104901.
- Issa, R., 1986. Solution of the implicitly discretised fluid flow equations by operator-splitting. *Journal of Computational Physics* 62, 40–65.
- Krajnović, S., Sarmast, S., 2010. LES of the flow around a generic wheel in a wheelhouse, in: 3rd Joint US-European Fluids Engineering Summer Meeting, Montreal, Canada. FEDSM-ICNMM2010-30687.
- Krajnović, S., Davidson, L., 2005. Influence of floor motions in wind tunnels on the aerodynamics of road vehicles. *Journal of Wind Engineering and Industrial Aerodynamics* 93, 677 – 696. URL: <http://www.sciencedirect.com/science/article/pii/S0167610505000450>, doi:<https://doi.org/10.1016/j.jweia.2005.05.002>.
- Larchevêque, L., Sagaut, P., Lê, T.H., Comte, P., 2004. Large-eddy simulation of a compressible flow in a three-dimensional open cavity at high reynolds number. *Journal of Fluid Mechanics* 516, 265–301.
- Lorite-Diez, M., Jimenez-Gonzalez, J.I., Pastur, L., Martinez-Bazan, C., Cadot, O., 2020. Experimental analysis of the effect of local base blowing on three-dimensional wake modes. *Journal of Fluid Mechanics* 883, A53. doi:10.1017/jfm.2019.917.
- Lucas, J., Cadot, O., Herbert, V., Parpais, S., Delery, J., 2017. A numerical investigation of the asymmetric wake mode of a squareback ahmed body effect of a base cavity. *Journal of Fluid Mechanics* 831, 675 – 679.
- Mair, W., 1978. Drag-reducing techniques for axi-symmetric bluff bodies, in: *Aerodynamic drag mechanisms of bluff bodies and road vehicles*. Springer, pp. 161–187.
- Menter, F.R., 1994. Two-equation eddy-viscosity turbulence models for engineering applications. *AIAA journal* 32, 1598–1605.
- Meunier, P., Lewke, T., 2003. Analysis and treatment of errors due to high velocity gradients in particle image velocimetry. *Exp. fluids* 35, 408–421.
- Monty, J., Harun, Z., Marusic, I., 2011. A parametric study of adverse pressure gradient turbulent boundary layers. *International Journal of Heat and Fluid Flow* 32, 575 – 585. URL: <http://www.sciencedirect.com/science/article/pii/S0142727X11000452>, doi:<https://doi.org/10.1016/j.ijheatfluidflow.2011.03.004>. 8th International Symposium on Engineering Turbulence Modelling and Measurements, Marseille, France, June 9 to 11, 2010.
- Passaggia, P.Y., Chalamalla, V., Hurley, M.W., Scotti, A., Santilli, E., 2020. Estimating pressure and internal-wave flux from laboratory experiments in focusing internal waves. *Exp. Fluids* 61, 1–29.
- Passaggia, P.Y., Mazellier, N., Kourta, A., 2021. Aerodynamic drag modification induced by free-stream turbulence effects on a simplified road vehicle. *P. Fluids* 33, 105108.
- Pope, S.B., 2001. Turbulent flows. *Measurement Science and Technology* 12, 2020–2021. URL: <https://doi.org/10.1088/0957-0233/12/11/705>, doi:10.1088/0957-0233/12/11/705.
- Rhie, C.M., Chow, W.L., 1983. A Numerical Study of the Turbulent Flow Past an Airfoil with Trailing Edge Separation. *AIAA Journal* 21, 1525–1532.
- Roshko, A., 1955. On the wake and drag of bluff bodies. *Journal of the aeronautical sciences* 22, 124–132.
- Roshko, A., 1993a. Free shear layers, base pressure and bluff-body drag. Technical Report. California Inst of Tech Pasadena Graduate Aeronautical Labs.
- Roshko, A., 1993b. Perspectives on bluff body aerodynamics. *Journal of Wind Engineering and Industrial Aerodynamics* 49, 79–100.

- Serre, E., Minguéz, M., Pasquetti, R., Guilmineau, E., Deng, G.B., Kornhaas, M., Schäfer, M., Fröhlich, J., Hinterberger, C., Rodi, W., 2013. On simulating the turbulent flow around the ahmed body: A french–german collaborative evaluation of les and des. *Computers & Fluids* 78, 10 – 23. URL: <http://www.sciencedirect.com/science/article/pii/S0045793011001885>, doi:<https://doi.org/10.1016/j.compfluid.2011.05.017>. IES of turbulence aeroacoustics and combustion.
- Shanmughan, R., Passaggia, P.Y., Mazellier, N., Kourta, A., 2020. Optimal pressure reconstruction based on planar particle image velocimetry and sparse sensor measurements. *Experiments in Fluids* 61, 1–19.
- Spohn, A. & GILLIERON, P., 2002. Flow separations generated by a simplified geometry of an automotive vehicle. In Congress IUTAM Symposium on Unsteady Separated Flows (Toulouse, France, 8–12 April). .
- Stella, F., Mazellier, N., Joseph, P., Kourta, A., 2018. Mass entrainment-based model for separating flows. *Phys. Rev. Fluids* 3, 114702. URL: <https://link.aps.org/doi/10.1103/PhysRevFluids.3.114702>, doi:10.1103/PhysRevFluids.3.114702.
- Stella, F., Mazellier, N., Kourta, A., 2017. Scaling of separated shear layers: an investigation of mass entrainment. *Journal of Fluid Mechanics* 826, 851–887. doi:10.1017/jfm.2017.455.
- Tenaud, C., Fraigneau, Y., et al., 2011. Numerical simulation of the turbulent detached flow around a thick flat plate, in: *Computational Fluid Dynamics 2010*. Springer, pp. 317–323.
- Trip, R., Fransson, J.H., 2017. Bluff body boundary-layer modification and its effect on the near-wake topology. *Physics of Fluids* 29, 095105.
- Volpe, R., Devinant, P., Kourta, A., 2015. Experimental characterization of the unsteady natural wake of the full-scale square back ahmed body: flow bi-stability and spectral analysis. *Experiments in Fluids* 56, 99. URL: <https://doi.org/10.1007/s00348-015-1972-0>, doi:10.1007/s00348-015-1972-0.

CRedit authorship contribution statement

Wassim Zeidan: Performed experiments and simulations, and drafted the paper. **Nicolas Mazellier:** Conceptualised the research, drafted the manuscript, and directed experiments. **Emmanuel Guilmineau:** Conceptualised the research and directed the numerical simulations. **Pierre-Yves Passaggia:** Wrote the manuscript. **Azeddine Kourta:** Conceptualised the research, drafted the manuscript and directed the research program..